# Mechanochemical Synthesis Enables Melting, Glass Formation and Glass-Ceramic Conversion in a Cadmium-based Zeolitic Imidazolate Framework

Wen-Long Xue[1], Alexander Klein[2], Mounir El Skafi[3], Jan-Benedikt Weiß[1], Felix Egger[4], Hui Ding[5], Suresh K. Vasa[2], Christian Liebscher[5], Mirijam Zobel[4], Rasmus Linser[2], Jin-Chong Tan[3], Sebastian Henke[1]*

[1] Anorganische Chemie, Fakultät für Chemie und Chemische Biologie, Technische Universität Dortmund, Otto-Hahn Straße 6, 44227 Dortmund, Germany

[2] Physikalische Chemie, Fakultät für Chemie und Chemische Biologie, Technische Universität Dortmund, Otto-Hahn-Straße 4a, 44227 Dortmund, Germany

[3] Multifunctional Materials & Composites (MMC) Laboratory, Department of Engineering Science, University of Oxford, Parks Road, Oxford OX1 3PJ, United Kingdom

[4] Institute of Crystallography, RWTH Aachen University, Jägerstr. 17-19, 52066 Aachen, Germany

[5] Abteilung Struktur und Nano- / Mikromechanik von Materialien, Max-Planck-Institut für Nachhaltige Materialien GmbH, 40237 Düsseldorf, Germany.

## ABSTRACT

Metal-organic frameworks (MOFs) are versatile materials with tunable properties and broad applications. Here, we report the first cadmium-based zeolitic imidazolate framework (ZIF) glass, prepared by melt-quenching sub-micrometer-sized $Cd(im)_2$ particles ($im^-$ = imidazolate) obtained via mechanochemical synthesis. This route increases defect density and reduces crystallite domain size, lowering the melting temperature from 461 °C (for larger solution-synthesized microcrystals) to 455 °C, thereby mitigating thermal decomposition during melting. Crystalline $Cd(im)_2$ adopts a two-fold interpenetrated diamondoid (**dia-c**) topology, assembled from tetrahedral $Cd^{2+}$ centers and $im^-$ linkers. Rapid cooling yields a monolithic glass with a glass transition temperature ($T_g$) of 175 °C. Structural analysis confirms that short-range connectivity within individual networks is maintained, whereas interactions between the interpenetrated networks are disrupted. Upon reheating, partial recrystallization produces a single-component glass-ceramic with enhanced mechanical properties, an unprecedented behavior in melt-quenched ZIF glasses. Investigations of thermal parameters (cooling rates) and partial linker substitution reveal strategies for tuning the phase behavior of both glass and glass-ceramic. These findings extend ZIF glass systems to second-row transition metal ions and underscore mechanochemical synthesis as a tool for tailoring the thermal properties of MOFs. This dual-phase functionality, combining glassy and crystalline domains of identical composition within a single material, offers potential for applications in thermal energy storage, phase change memory, and optics.

## INTRODUCTION

Zeolitic imidazolate framework (ZIF) glasses,[1-3] a subset of metal-organic framework (MOF) and coordination polymer (CP) glasses,[4-5] possess continuous random network structures underpinned by Werner-type coordination chemistry.[6-7] These materials combine the advantageous chemical functionality and porosity of their crystalline ZIF counterparts with exceptional processability[8-12], even enabling the preparation of micro-optical elements for sensing applications[13]. These unique attributes make ZIF glasses highly attractive for diverse applications, ranging from molecular separation[14-15] and solid-state ion conduction[16] to optoelectronics[17]. Despite the large variety of crystalline ZIFs reported to date,[18-19] only a small fraction can be melted and transformed into glasses by melt-quenching. The melting process involves the dynamic breaking and reorganization of the metal–imidazolate coordination bonds, a phenomenon currently limited to ZIFs based on the first-row transition metal ions such as $Zn^{2+}$, $Co^{2+}$, and $Fe^{2+}$, and a few network topologies (i.e., **cag**, **zni**, **gis**, **sod**, **afi**, and **can**).[3, 10,20-22] For most other crystalline ZIFs, including the $Cu^{2+}$-based system $Cu(im)_2$ ($im^-$ = imidazolate),[23] the organic imidazolate-type linkers decompose before or during the melting process, presenting a significant challenge to expanding the library of meltable ZIFs.

To overcome this limitation, extensive efforts have focused on lowering the melting points of crystalline ZIFs to enable their liquefaction at reduced temperatures, thereby facilitating glass formation via melt-quenching. The most prevalent approach to lower the melting temperatures of these materials is the incorporation of functionalized linkers with weaker metal coordination bonds, such as benzimidazolate, 4,5-dicyanoimidazolate, and purinate,[2, 15, 24] so that the crystals melt at a lower temperature. Moreover, mechanical perturbation is thought to introduce structural defects within ZIFs, further lowering their melting points.[23] Applying high hydrostatic pressure[25] or high-frequency vibration[26] to crystalline ZIFs also promotes melting at lower temperatures. In addition, mechanochemistry has emerged as a powerful strategy not only for lowering the melting points of crystalline ZIFs[2, 27] but also for directly synthesizing glassy ZIF powders that are otherwise inaccessible through conventional methods.[23, 28] In the case of crystalline ZIFs, mechanochemical synthesis typically yields microcrystals with significantly smaller particle sizes and increased structural disorder compared to those produced via conventional solvothermal methods. These features are strongly correlated with enhanced meltability, as they facilitate bond rearrangement and lower the energy barrier for melting. For example, mechanochemically synthesized crystalline ZIF-62 exhibits a significantly lower melting temperature compared to its solvothermally synthesized counterpart.[27]

In this work, driven by the goal of expanding the as-of-yet very small family of meltable ZIFs, we demonstrate the first meltable cadmium-based ZIF based on the literature-known $Cd(im)_2$, which adopts a two-fold interpenetrated (catenated) diamondoid topology **dia-c**. While solution-synthesized $Cd(im)_2$ thermally decomposes concurrently with melting, mechanochemically synthesized $Cd(im)_2$ exhibits smaller crystallite domain sizes along with a higher density of structural defects, thereby affording a larger separation between its melting and decomposition temperatures. This separation enables the preparation of a melt-quenched $Cd(im)_2$ glass with minimal decomposition. Remarkably, upon rapid quenching, liquid $Cd(im)_2$ transitions into a ZIF glass that undergoes partial recrystallisation upon reheating, forming a semitransparent single-component glass-ceramic with enhanced mechanical properties. This controlled partial recrystallization within the glass matrix, resulting in the formation of the first ZIF glass-ceramic, is a distinctive feature of the $Cd(im)_2$ system and has not been observed in the previously reported ZIF glasses based on first-row transition metals.

## RESULTS AND DISCUSSION

### Materials preparation, crystallographic and thermal characterization

Crystalline $Cd(im)_2$ was synthesized via two distinct methods: a solution-based route from $Cd(NO_3)_2{\cdot}4H_2O$ and imidazole (imH), as previously reported,[29] and the newly developed mechanochemical ball-milling approach from CdO and imH (Figure 1a and Supporting Information Section 1). The resulting ZIF materials are referred to as $Cd(im)_2$-*sol* (solution-synthesized) and $Cd(im)_2$ (mechanochemically synthesized). Both $Cd(im)_2$ variants crystallize in the same structure, featuring the two-fold interpenetrated **dia-c** topology and share the same composition, with $Cd^{2+}$ as the inorganic nodes and $im^-$ as the organic linkers. After washing, the dried $Cd(im)_2$ materials were obtained by heating to 150 °C under dynamic vacuum for 6 h. Complete removal of residual solvents was confirmed by Fourier-transform infrared (FTIR) spectroscopy of the solid ZIFs and solution $^1$H nuclear magnetic resonance ($^1$H NMR) spectroscopy of acid-digested samples (see Supporting Information Section 6-7).

The identity and purity of the crystalline $Cd(im)_2$ materials were verified by structureless profile fits (Pawley refinements) of powder X-ray diffraction (PXRD) patterns, using reference crystallographic data from the literature[29] (Figures 1b, S6-S7 and Table S3). Average crystallite domain sizes were determined from the integral breadth of the Bragg peaks in the PXRD patterns using Scherrer's equation and a combined Gaussian-Lorentzian (Voigt-type) peak broadening model as implemented in TOPAS academic v6. This analysis reveals that mechanochemically synthesised $Cd(im)_2$ exhibits a substantially smaller average domain size

(47.3 ± 0.9 nm) compared to Cd(im)$_2$-*sol* (>1000 nm). Transmission electron microscopy (TEM) further corroborated these findings, showing particle sizes below 500 nm for Cd(im)$_2$ in contrast to ~2 µm for Cd(im)$_2$-*sol* (Figure S3). The markedly smaller domain sizes observed for the mechanochemically synthesized Cd(im)$_2$ suggest a higher density of structural defects, especially at grain boundaries and particle surfaces, compared to the highly crystalline solution-synthesized counterpart.

Simultaneous thermogravimetry and differential thermal analysis (TG/DTA) was performed on both Cd(im)$_2$ and Cd(im)$_2$-*sol* under a $N_2$ atmosphere with a heating rate of +10 °C min$^{-1}$. TG data show that thermal decomposition begins at 473 °C for Cd(im)$_2$ and at 455 °C for Cd(im)$_2$-*sol* (Figures 1c and S43). These decomposition temperatures ($T_d$) are significantly lower than those observed for ZIF-4(Zn) (Zn(im)$_2$, 605 °C)[23], ZIF-4(Co) (Co(im)$_2$, 546 °C)[23] and MUV-24(zni) (Fe(im)$_2$, 530 °C)[21]. The DTA trace of Cd(im)$_2$ exhibits a pronounced endothermic signal at 447 °C (peak temperature), corresponding to the melting of the framework (Figure 1c). While the DTA of Cd(im)$_2$-*sol* also displays a comparable melting signal, it overlaps with its $T_d$ (Figure S43), preventing access to a stable liquid phase. In contrast, the mechanochemically synthesized Cd(im)$_2$ benefits from the smaller crystallite domain sizes and increased defect density (particularly surface defects), achieving a liquid phase with minimal decomposition. This highlights a key advantage of the mechanochemical synthesis approach: it enables liquefaction at a lower temperature by reducing the energy barrier for melting, a consequence of reduced crystallite domain sizes and increased structural defect densities.

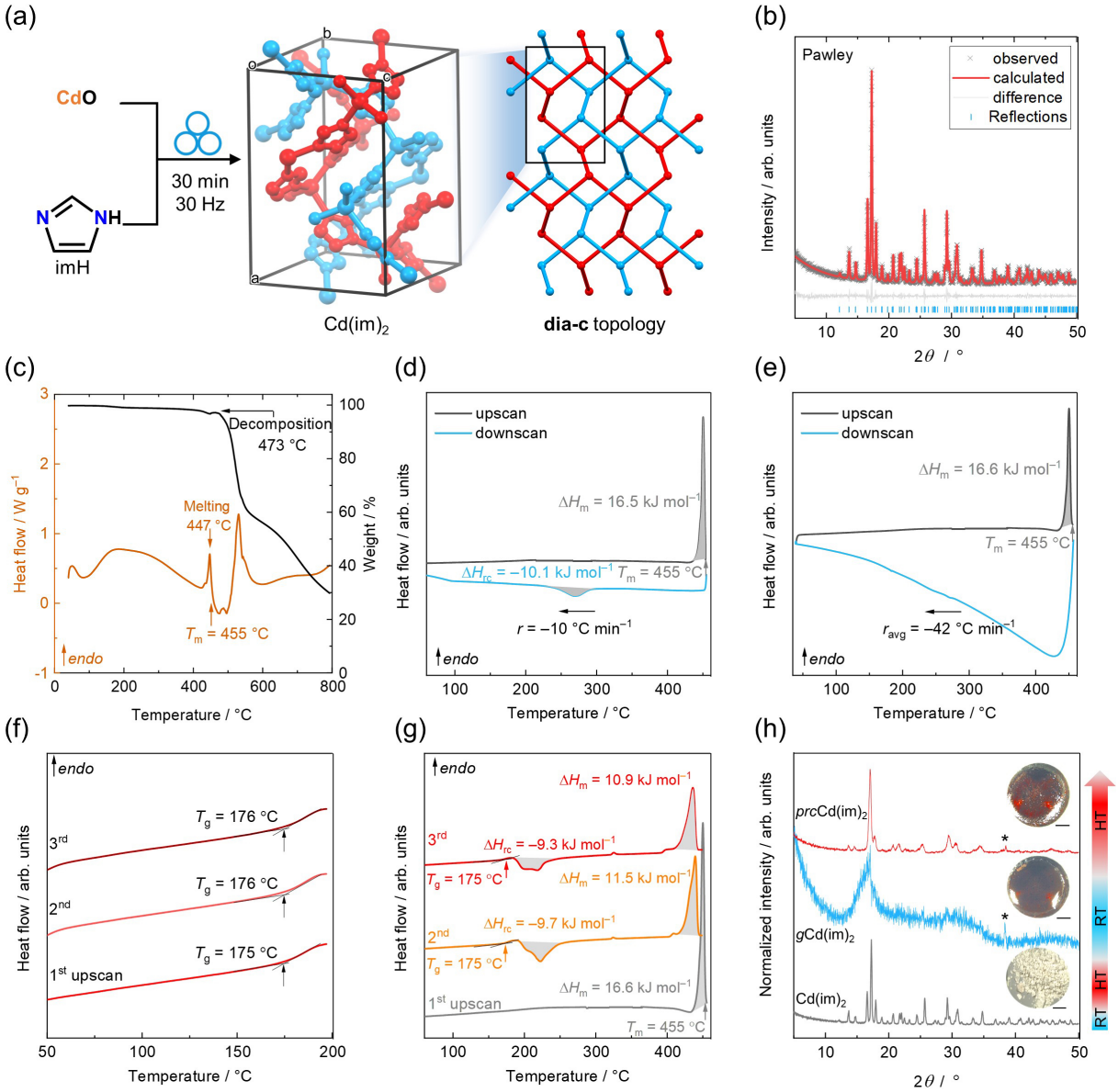


**Figure 1.** (**a**) Scheme of the mechanosynthetic route to $Cd(im)_2$ and its **dia-c** topology. Hydrogen atoms are omitted for clarity. The two interpenetrated networks are depicted in red and blue, respectively. (**b**) Profile fit (Pawley method) performed on the PXRD pattern of $Cd(im)_2$. (**c**) TG/DTA trace of $Cd(im)_2$ recorded with a +10 °C $min^{-1}$ heating rate. (**d-e**) DSC curves of $Cd(im)_2$ with (average) cooling rates of –10 °C $min^{-1}$ and –42 °C $min^{-1}$. (**f**) Three consecutive DSC cycles for *g*$Cd(im)_2$ showcasing the stability of $T_g$. The heating and cooling rates for all scans were ±10 °C $min^{-1}$. (**g**) Three cyclic DSC of $Cd(im)_2$ with a heating rate of +10 and an average cooling rate of –42 °C $min^{-1}$. The weak endothermic signal at 325 °C is associated to the melting of metallic cadmium. (**h**) Normalized PXRD patterns of $Cd(im)_2$, *g*$Cd(im)_2$, and *prc*$Cd(im)_2$. The reflection marked with an asterisk corresponds to the trace decomposition product Cd metal. The insets show micrographs of the corresponding samples. All scale bars are 1 mm.

To gain deeper insights into the thermal phase changes during heating and cooling cycles, cyclic differential scanning calorimetry (DSC) experiments were conducted between ambient

temperature and $T_d$ under an inert $N_2$ atmosphere. Upon heating, the melting of $Cd(im)_2$ is completed at a melting temperature ($T_m$) of 455 °C (peak offset). The enthalpy of fusion ($\Delta H_m$) amounts to about 17 kJ $mol^{-1}$, significantly higher than $\Delta H_m$ of $Zn(im)_2$ (ca. 12 kJ $mol^{-1}$).[11] Notably, the substantial difference in $\Delta H_m$ cannot be attributed to the chemical bond strength between the different metal centers and the $im^-$ linkers. Density functional theory (DFT) calculations of molecular model complexes suggest that the Cd–N bond strength is substantially weaker than the Zn–N bond strength (see Figure S5 and Table S2). Instead, the higher $\Delta H_m$ of $Cd(im)_2$ can be attributed to its denser crystal packing, which results in stronger dispersion interactions due to the two-fold interpenetration of the framework. The interpenetrated **dia-c** topology of $Cd(im)_2$ features a substantially higher metal ion density (5.13 $Cd^{2+}$ ions per $nm^3$) compared to the more open **zni** topology network exhibited by $Zn(im)_2$ (4.66 $Zn^{2+}$ ions per $nm^3$) (Figure S1).[29-30] This denser structure enhances the cohesive energy of $Cd(im)_2$, thereby accounting for its higher $\Delta H_m$.

During cooling of the liquid $Cd(im)_2$ to room temperature with a rate of −10 °C $min^{-1}$, the material undergoes partial recrystallisation, forming a mixed amorphous/crystalline material (Figure 1d and S15). Upon further heating to 300 °C at a rate of +10 °C $min^{-1}$, the material fully recrystallizes into the original **dia-c** phase. The fully recrystallized sample obtained after reheating to 300 °C is termed *frc*$Cd(im)_2$ (*frc* denotes fully recrystallized) (Figures S9 and S41). Importantly, faster cooling rates effectively suppress recrystallization. When the fastest cooling rate of the used DSC instrument is applied (with an actual average rate of approximately –42 °C $min^{-1}$ from $T_m$ to $T_g$ is due to instrumental limitations; Figure S39), liquid $Cd(im)_2$ forms a compact monolithic glass, termed *g*$Cd(im)_2$ (Figure 1e and insert in Figure 1h). This transition is evidenced by the absence of Bragg scattering in the PXRD patterns (Figures 1h and S13) and the observation of a glass transition signal at 175 °C ($T_g$ = glass transition temperature) during a subsequent heating scan. The consistent $T_g$ values (175–176 °C) observed across three consecutive upscans demonstrate that *g*$Cd(im)_2$ exhibits good resistance against recrystallization during thermal cycling (Figure 1f). Furthermore, a sample of *g*$Cd(im)_2$ stored under ambient conditions for 90 days shows no signs of recrystallization, further confirming the long-term stability of the glassy phase (Figure S13). Heat capacity ($C_p$) measurements reveal that the heat capacity change at the glass transition ($\Delta C_p$) of *g*$Cd(im)_2$ is 0.16 J $K^{-1}$ $g^{-1}$ (Figure S49), comparable to values reported for other ZIF glasses (Table S6). Furthermore, analysis of the variation in fictive temperature ($T_f$) with the different cooling rates allowed for the determination of the dimensionless calorimetric fragility index ($m$) of the supercooled liquid.[2] Within measurement error, $m$ is about 43 (Figure S50), which is much higher than the fragility indices of prototypical $Zn^{2+}$-based glasses such as $a_T$ZIF-4 ($m$ = 31) and $a_g$ZIF-62 ($m$

= 24, Figure S51).[2, 31] This elevated fragility index suggests that *g*Cd(im)$_2$ is a more ductile glass, suitable for specific applications typically dominated by organic polymers.

Notably, *g*Cd(im)$_2$-*sol*, which was prepared at a higher temperature due to its higher $T_m$, contains metallic Cd, as detected by PXRD (Figures S12). We suppose some im$^-$ linkers decompose during the melting of Cd(im)$_2$-*solv*, and their decomposition products promote the reductive formation of metallic Cd particles in the Cd(im)$_2$ glass matrix. A similar phenomenon has been reported previously for a $Co^{2+}$-based ZIF glass.[20] By contrast, the mechanically synthesized Cd(im)$_2$ effectively minimizes this undesirable effect during melting, yielding only trace amounts of metallic Cd in *g*Cd(im)$_2$ according to PXRD and DSC data (Figures 1h, S13 and S40). This improvement can be attributed to the smaller crystallite domain size and the higher defect density of mechanochemically synthesized Cd(im)$_2$, which lowers its $T_m$ compared to Cd(im)$_2$-*sol*, thereby reducing the extent of thermal decomposition and metallic Cd formation.

Strikingly, upon reheating *g*Cd(im)$_2$, partial recrystallization occurs between 200 and 260 °C, where the supercooled liquid partially crystallizes into the original Cd(im)$_2$ structure with the **dia-c** topology. This process is confirmed by DSC, *in situ* and *ex situ* PXRD (Figures 1g, 1h, S8 and S11). The enthalpy of recrystallization ($\Delta H_{rc}$) is approximately –9.7 kJ mol$^{-1}$, suggesting that about 59% of the material undergoes cold crystallization. The material derived after reheating *g*Cd(im)$_2$ to 300 °C is referred to as *prc*Cd(im)$_2$ (*prc* = partially recrystallized). Remarkably, despite a large fraction of the sample having recrystallized, *prc*Cd(im)$_2$ retains the monolithic, semitransparent morphology of *g*Cd(im)$_2$ (Figures 1h and S53). Crystallite domain size analysis, based on the peak widths of the Bragg reflections in the PXRD pattern, suggests an average domain size of only 19.0(6) nm (Table S3), indicating that *prc*Cd(im)$_2$ is composed of nanocrystalline grains embedded within a glassy matrix of the same composition.

The semitransparent nature of the monolithic *prc*Cd(im)$_2$ implies strong interfacial bonding between the nanocrystalline grains and the surrounding glass matrix. This unique microstructure, characterized by seamless integration of amorphous and crystalline regions, is a defining hallmark of glass-ceramics.[32] Notably, *prc*Cd(im)$_2$ represents the first example of such complex semi-crystalline materials in the realm of MOFs. Furthermore, the transitions between the crystalline, liquid and partially recrystallized glass-ceramic phases are highly reproducible across multiple heating and cooling cycles, demonstrating excellent repeatability of the processes involved (Figure 1g).

Interestingly, the nanocrystalline Cd(im)$_2$ phase within *prc*Cd(im)$_2$ exhibits an expanded unit cell volume of 1611(2) Å$^3$ at room temperature, which is significantly larger than the unit cell volume of mechanochemically synthesized Cd(im)$_2$ under the same conditions (1565.4(2) Å$^3$)

(Figure S8 and Table S3). Crystalline $Cd(im)_2$ is known for its anomalously large thermal expansion, with a unit cell volume increase of about 5.4% between 100 and 500 K (Figure S2).[29] Hence, the 2.9% larger unit cell volume of the nanocrystallites of *prc*$Cd(im)_2$ compared to the unit cell volume of the $Cd(im)_2$ crystallites at room temperature, suggests that these crystallites, which form during the growth process at temperatures between 200 to 260 °C, are strongly encapsulated within the surrounding glass matrix. This encapsulation restricts their relaxation to the more compact unit cell configuration typically observed in fully crystalline $Cd(im)_2$ at ambient conditions. As a result, the nanocrystallites of *prc*$Cd(im)_2$ retain a larger unit cell volume at room temperature. This phenomenon is conceptually analogous to the stabilization of high-temperature phases of the perovskite $CsPbI_3$ and the MOF MIL-53 by encapsulation within ZIF glass matrices, where interfacial strain and nanoscale confinement suppress phase transitions toward thermodynamic equilibrium.[17, 33] The unprecedented transition from the glassy state to a glass-ceramic state, featuring nanocrystal encapsulation and robust interfacial bonding, has not been observed in previous studies on ZIF glasses, underscoring the unique properties of the $Cd(im)_2$ system.

**High-resolution transmission electron microscopy**

To shed light on the interfacial contact between the crystalline and amorphous domains of the glass-ceramic, high-resolution transmission electron microscopy (HR-TEM) imaging of *prc*$Cd(im)_2$ was conducted (Figure 2a). The analysis faced challenges due to the electron beam sensitivity of the material and the limited contrast between the crystalline nanoparticles and the amorphous matrix. Despite these difficulties, HR-TEM imaging successfully revealed a distinct crystalline nanoregion embedded within the glass matrix, consistent with the growth of $Cd(im)_2$ nanocrystals from the supercooled liquid phase above $T_g$. The crystalline domain exhibits well-defined lattice fringes with a spacing of 0.35 nm (Figure 2a). This fringe spacing was further validated by Fast Fourier Transform (FFT) analysis (Figure S4), which confirms excellent agreement with the (302) lattice plane spacing of the known $Cd(im)_2$ crystal structure (Figure 2b). Remarkably, the boundary between the crystalline and amorphous regions appears diffuse in the HR-TEM image, lacking a sharp interface. This observation aligns with the previous interpretation of the PXRD and DSC results and suggests a high degree of structural continuity between the two phases. The seamless fusion of crystalline and glassy regions can be attributed to the chemical homogeneity of the system, as both phases share the same chemical composition of $Cd(im)_2$.

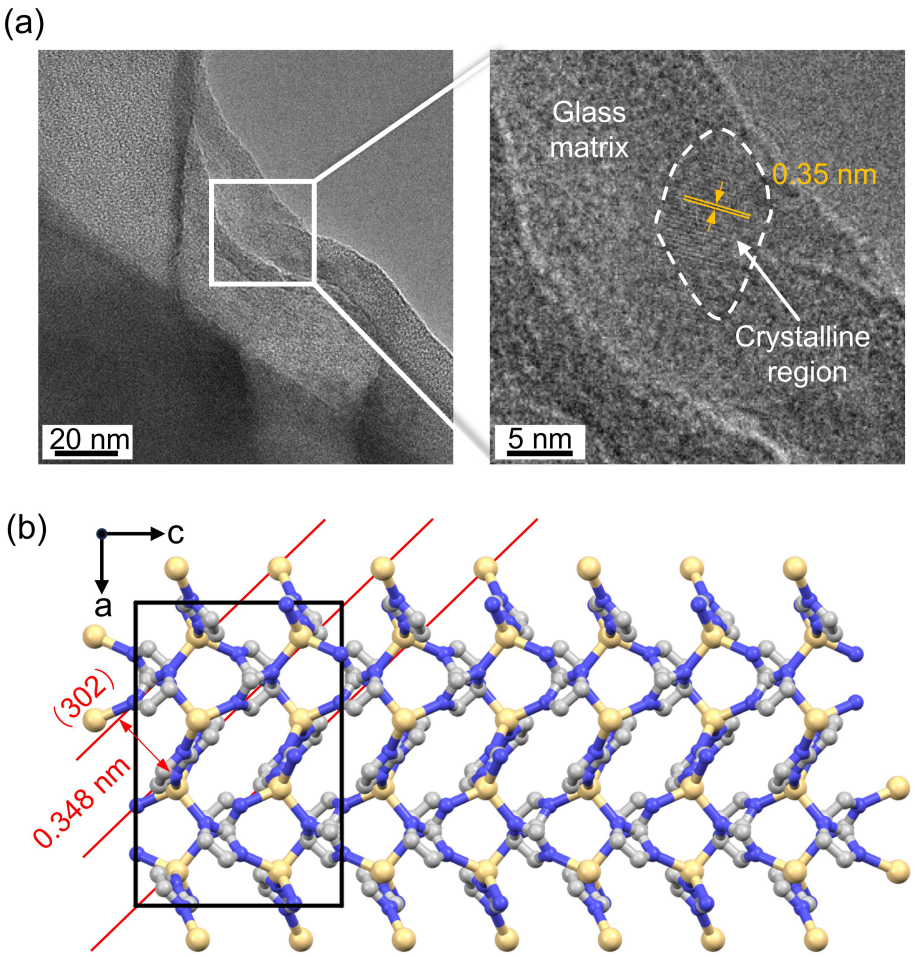


**Figure 2.** (**a**) HR-TEM images with two different magnifications of *prc*Cd(im)$_2$. (**b**) Schematic illustration of the (302) crystal planes within the Cd(im)$_2$ framework taken from CCDC code BAYQAU11, viewed along the crystallographic *b* axis. The Cd, N, and C atoms are shown as yellow, blue, and gray spheres, respectively. Hydrogen atoms are omitted for clarity.

## Local structure analysis

To gain deeper insights into the local structural changes occurring during the transitions between the crystalline, glassy, and glass-ceramic phases of Cd(im)$_2$, Fourier transform infrared (FTIR) spectra were recorded for all four samples, Cd(im)$_2$, *g*Cd(im)$_2$, *prc*Cd(im)$_2$, and *frc*Cd(im)$_2$, in both the mid- and far-infrared regions. These measurements allow tracking of structural distortions, disorder, and recovery at the molecular level. In line with the loss of long-range order, increased structural heterogeneity and distortions in *g*Cd(im)$_2$ are evident from the broadening of vibrational bands in the FTIR spectra relative to those of the crystalline parent Cd(im)$_2$ (Figure S35). This is particularly pronounced in the out-of-plane ring deformation modes[11, 34] of im$^-$ between 700 and 900 cm$^{-1}$ (Figure 3a) and the stretching vibration of the CdN$_4$ tetrahedra centred at 252 cm$^{-1}$ (Figure 3b). These vibrational bands become significantly broader after melt-quenching, reflecting the increased disorder in

*g*Cd(im)$_2$. The slight upshift of the out-of-plane ring deformation modes located around 750 cm$^{-1}$ upon vitrification likely indicates subtle differences in local structural environments between the crystalline and glassy phases. As the structure transitions from *g*Cd(im)$_2$ to *prc*Cd(im)$_2$ and finally to *frc*Cd(im)$_2$, the vibrational bands gradually sharpen, consistent with the partial and complete recovery of structural order in the glass-ceramic and fully recrystallized phases. Notably, the stretching vibration of $CdN_4$ is located at a much lower frequency (252 cm$^{-1}$) compared to $ZnN_4$ (301 cm$^{-1}$) and $CoN_4$ (331 cm$^{-1}$) in ZIF-4(Zn) and ZIF-4(Co), respectively.[23] This difference can be attributed to the higher mass of $Cd^{2+}$, which reduces the vibrational frequency. Additionally, the lower frequency indicates a weaker Cd–N bond strength compared to Zn–N and Co–N bonds, as suggested by density functional theory (DFT) calculations of molecular model complexes (Figure S5 and Table S2).

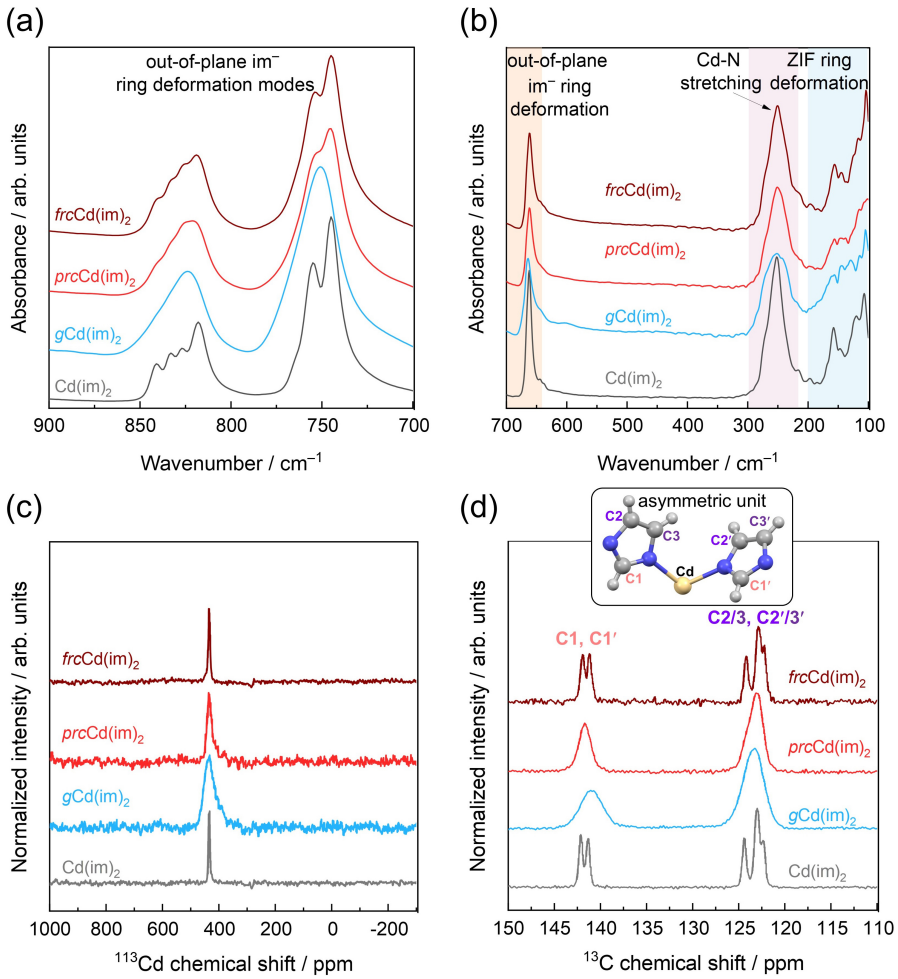


**Figure 3.** FTIR spectra in the range from 700 – 900 cm$^{-1}$ (**a**) and 100 - 700 cm$^{-1}$ (**b**) of Cd(im)$_2$, *g*Cd(im)$_2$, *prc*Cd(im)$_2$, and *frc*Cd(im)$_2$. (**c**) $^{113}$Cd MAS NMR and (**d**) $^{13}$C MAS NMR of Cd(im)$_2$, *g*Cd(im)$_2$, *prc*Cd(im)$_2$, and *frc*Cd(im)$_2$. The inset shows the asymmetric unit of Cd(im)$_2$, taken from the reported crystal structure (CCDC code BAYQAU11). The Cd, N, and C atoms are shown as yellow, blue, and gray spheres, respectively.

To complement the FTIR analysis, solid-state magic angle spinning nuclear magnetic resonance (MAS NMR) spectroscopy was performed to probe the local structural environment further. MAS NMR is particularly powerful for studying disordered and amorphous materials, as it provides direct information on short-range order and disorder, especially when targeting the NMR-active nuclei of metal centers. While MAS NMR investigations of the $Fe^{2+}$-, $Co^{2+}$-, and $Cu^{2+}$-derivatives of ZIF glass formers are limited due to paramagnetism, low sensitivity and low abundance, $Cd(im)_2$ offers a distinct advantage: the $^{113}Cd$ nucleus (spin 1/2) exhibits no quadrupolar effect, enabling high-resolution spectra with sharp resonances. In contrast to $^{67}Zn$, which requires ultra-high magnetic fields and suffers from extremely broad line shapes over a very wide chemical shift range due to its quadrupolar nature,[35] $^{113}Cd$ allows for significantly more straightforward analysis.

Accordingly, $^{113}Cd$ MAS NMR spectra were recorded for $Cd(im)_2$, *g*$Cd(im)_2$, *prc*$Cd(im)_2$, and *frc*$Cd(im)_2$ to investigate structural changes (Figure 3c). Additionally, $^{13}C$ MAS NMR spectra were recorded to provide complementary insights into the organic building blocks (Figure 3d). The $^{113}Cd$ MAS NMR spectrum of crystalline $Cd(im)_2$ features a sharp, symmetrical resonance at 433 ppm, consistent with the presence of a single crystallographically independent $Cd^{2+}$ site. In contrast, the spectrum of *g*$Cd(im)_2$ shows a much broader and asymmetric line shape, indicative of significant short-range structural heterogeneity in the glassy phase. This heterogeneity arises from variations in bond angles and local environments, analogous to findings in $^{29}Si$ MAS NMR studies of silicate glasses.[36] The $^{13}C$ MAS NMR spectra further corroborate these observations. Crystalline $Cd(im)_2$ exhibits six sharp resonances (two of them overlapping), corresponding to the six crystallographically unique carbon atoms. After glass formation, these resonances converge into two broader signals, reflecting the disordered environment in *g*$Cd(im)_2$. Upon partial recrystallization to *prc*$Cd(im)_2$, the signals in both $^{113}Cd$ and $^{13}C$ MAS NMR spectra sharpen, indicating partial recovery of structural order. Finally, after complete recrystallization to *frc*$Cd(im)_2$, the NMR spectra closely resemble those of the pristine crystalline $Cd(im)_2$, demonstrating the full restoration of order in the structure (Figure 3d).

Building on the insights gained from FTIR and MAS NMR spectroscopy, X-ray total scattering experiments were conducted to further explore the similarities and differences between the local atomistic structures of the various phases of $Cd(im)_2$. The total scattering structure factors, $S(Q)$, reveal that the Bragg peaks at low-$Q$, characteristic of crystalline $Cd(im)_2$, are not entirely absent for the glassy phase *g*$Cd(im)_2$ (Figure 4a). This observation can be attributed to two possible phenomena: (i) a small degree of recrystallization occurs from the $Cd(im)_2$ supercooled liquid even under the fastest cooling rate achievable with our DSC instrumentation, or (ii) the material has not fully melted at the maximum temperature

(457 °C) of the DSC run used to prepare the glass sample. To further investigate this, a glass sample of $Cd(im)_2$ was prepared by heating the material to a higher temperature (465 °C, first upscan in Figure S42) followed by rapid quenching. The resulting glass sample, denoted as *g*$Cd(im)_2$-*overheated*, exhibits no detectable Bragg peaks for crystalline $Cd(im)_2$ in its $S(Q)$ (Figure S24). However, larger amounts of crystalline Cd and CdO (presumably formed by the oxidation of metallic Cd nanoparticles upon exposure to air) are observed in the $S(Q)$ of *g*$Cd(im)_2$-*overheated*. This highlights the narrow temperature range between the melting and decomposition of $Cd(im)_2$, where overheating facilitates complete melting but also accelerates decomposition.

Pair distribution functions (PDFs) in the form $D(r)$ were calculated from the X-ray total scattering data to analyze the atomistic structure of $Cd(im)_2$ and its glassy and glass-ceramic phases (Figure 4c-e). To assign the peaks in the PDFs, partial and total PDFs for the constituent atom pairs of $Cd(im)_2$ were calculated using the PDFgui software.[37] The seven sharp features observed below 8 Å in the PDFs were assigned accordingly (Figure S19-20). Interestingly, a PDF peak corresponding to a Cd···Cd distance $r$ = 5.2 Å is observed in $Cd(im)_2$ (Figure 4c and Figure S19-20), which is not found in other reported ZIFs.[3, 10] This unique feature arises from the two-fold interpenetrated **dia-c** topology of $Cd(im)_2$, where the closer intermolecular (inter-network) Cd···Cd distance of 5.2 Å coexists with a longer intramolecular (intra-network) Cd···Cd distance across the $im^-$ linkers (6.4 Å) (Figure 4b). Additionally, the interpenetrated structure gives rise to another PDF peak at 6.8 Å, which is also attributed to intermolecular Cd···Cd correlations (Figure 4b- c and S19 -20). The PDF of *g*$Cd(im)_2$ illustrates that while the intra-network short-range order, specifically the Cd–im–Cd connectivity at 6.4 Å (correlation 6 in Figure 4c), remains preserved in the glass, the characteristic inter-network Cd···Cd correlations are significantly reduced in intensity (correlations 5 and 7 in Figure 4c). This implies that the interpenetrated structure is disrupted during the melting and glass formation processes, leading to substantial short-range disorder in *g*$Cd(im)_2$. In *prc*$Cd(im)_2$, the PDF shows that the short-range and long-range orders are only partially restored, reflecting the mixed crystalline/amorphous nature of the glass-ceramic (Figure 4d). Additional X-ray total scattering data collected during heating of *g*$Cd(im)_2$ demonstrate the gradual recovery of the inter-network Cd···Cd correlations during heating across the glass transition and cold-crystallization temperatures (Figure S21 -22). As expected, the PDF of *frc*$Cd(im)_2$ is nearly identical to that of $Cd(im)_2$, confirming the complete recovery of both short- and long-range orders (Figure 4e).

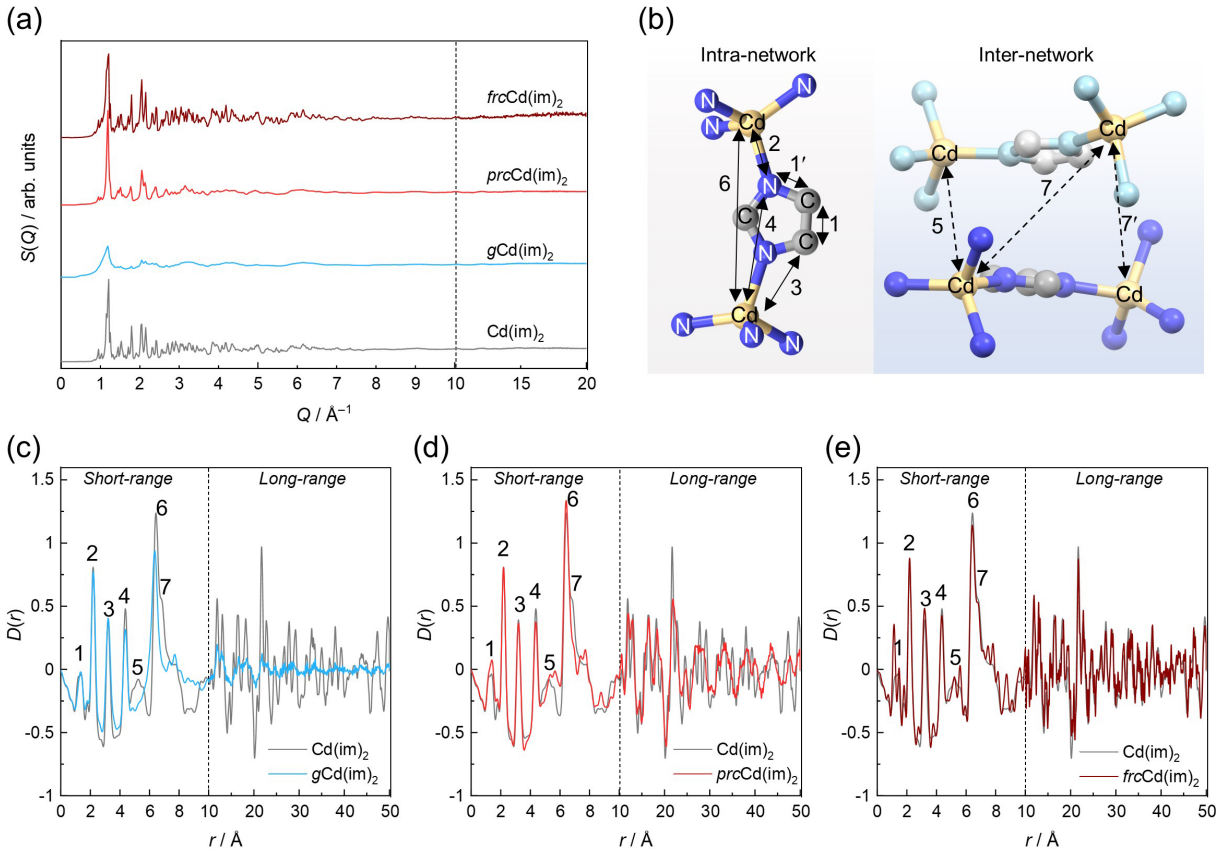


**Figure 4.** (**a**) X-ray total scattering data in the form of *S*(*Q*) of $Cd(im)_2$, *g*$Cd(im)_2$, *prc*$Cd(im)_2$, and *frc*$Cd(im)_2$. The *Q*-axis below 10 Å$^{-1}$ is displayed magnified to show the variation of the scattering function in more detail. (**b**) Visualization of the relevant short-range atomic distances (intra-network and inter-network) present in the $Cd(im)_2$ taken from the literature (CCDC code BAYQAU11). Assignment of the seven sharp features below 7 Å was carried out by using the PDFgui software[37] to calculate the partial and total PDFs for the constituent atom pairs of $Cd(im)_2$. The Cd, N, and C atoms are shown as yellow, blue, and gray spheres, respectively. Hydrogen atoms are omitted for clarity. The color of atoms from the second (interpenetrating) network is lightened for better discrimination. Comparison of PDF data of (**c**) $Cd(im)_2$ and *g*$Cd(im)_2$, (**d**) $Cd(im)_2$ and *prc*$Cd(im)_2$, and (**e**) $Cd(im)_2$ and *frc*$Cd(im)_2$ derived from the X-ray total scattering data. The *Q*-axis below 10 Å is displayed magnified.

## Mechanical properties

The mechanical properties of glass and glass-ceramic materials play a critical role in their suitability for various structural and functional applications.[38] In conventional inorganic glasses, glass-ceramics typically exhibit superior mechanical performance compared to their fully amorphous counterparts, owing to the presence of embedded crystalline domains, which enhance stiffness, hardness, and fracture resistance.[33, 39-40] To evaluate whether similar trends hold for the MOF-based $Cd(im)_2$ system, we systematically investigated the mechanical properties of *g*$Cd(im)_2$ glass and *prc*$Cd(im)_2$ glass-ceramic via nanoindentation (Figure 5 and Supporting Information Sections 1 and 11).[9, 33, 41]

Across the entire indentation depth range plotted (200–2000 nm), *prc*Cd(im)$_2$ consistently demonstrates higher reduced modulus ($E_r$) and hardness ($H$) compared to the *g*Cd(im)$_2$ (Figure 5). Specifically, the averaged $E_r$ and $H$ of *prc*Cd(im)$_2$ are 7.52 ± 0.41 GPa and 839 ± 54 MPa, respectively, significantly exceeding the values of 6.45 ± 0.45 GPa and 744 ± 97 MPa observed for *g*Cd(im)$_2$. Under the assumption of a Poisson's ratio ($\nu$) of 0.2 (0.4), the calculated Young's modulus ($E$) is 7.22 ± 0.39 GPa (6.32 ± 0.34 GPa) for *prc*Cd(im)$_2$, significantly higher than $E$ of *g*Cd(im)$_2$ (6.19 ± 0.43 GPa for $\nu$ = 0.2, 5.42 ± 0.38 GPa for $\nu$ = 0.4). In general, the values of $E$ and $H$ of the Cd(im)$_2$-based glass and glass-ceramic are comparable to those previously reported for ZIF glasses exhibiting first-row transition metal ions (Table S7). Notably, our results highlight the significant enhancement in mechanical properties achieved through partial recrystallization, highlighting the mechanical reinforcement of *prc*Cd(im)$_2$ by the embedded nanocrystals. The findings also establish a direct link between the microstructure and mechanical performance, consistent with trends observed in conventional glass-ceramics, where embedded crystalline domains contribute to improved mechanical properties.

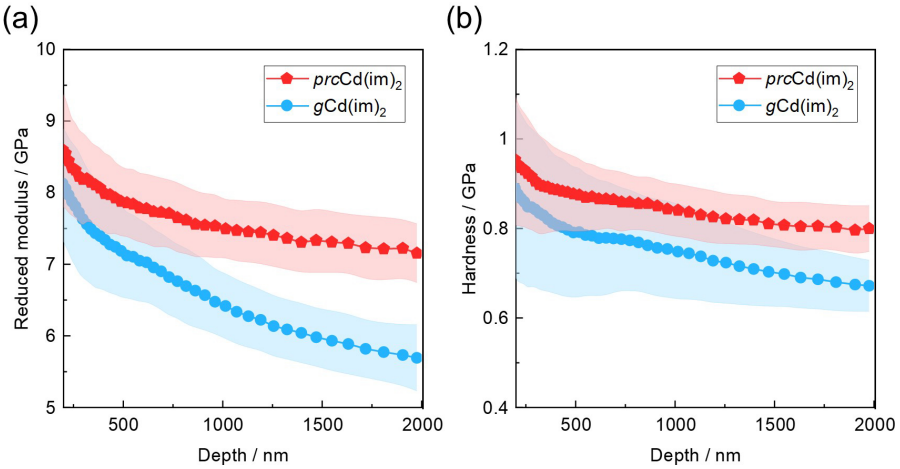


**Figure 5.** Variation of (**a**) reduced modulus $E_r$ and (**b**) hardness $H$ as a function of surface penetration depth of the Berkovich indenter into the *g*Cd(im)$_2$ glass and *prc*Cd(im)$_2$ glass-ceramic. The standard deviations are shaded in the corresponding colors.

### Comparison of Cd(im)$_2$ with other M(im)$_2$ glass formers

The thermal properties of Cd(im)$_2$ are distinct from those of previously studied M(im)$_2$ glass formers based on 3d transition metals ($M^{2+}$). While Co(im)$_2$ (**zni** topology) and Cu(im)$_2$ (**sod** topology) decompose upon melting ($T_d$ = 550 °C for Co(im)$_2$; $T_d$ = 258 °C for Cu(im)$_2$),[20, 23] Cd(im)$_2$ undergoes a distinct melting transition at 455 °C, enabling glass formation by melt-quenching. In contrast, Fe(im)$_2$ and Zn(im)$_2$ feature rather high thermal stability and melt with minimal decomposition at 482 °C and 590 °C, respectively.[1, 21] Despite its more densely packed interpenetrated framework structure, Cd(im)$_2$ (**dia-c** topology) has a lower melting

point than $Fe(im)_2$ and $Zn(im)_2$ (both **zni** topology), suggesting a weaker Cd–N bond strength compared to Fe–N and Zn–N interactions. This trend is further reflected in the lower $T_g$ of *g*$Cd(im)_2$ (175 °C) compared to $Fe(im)_2$ glass (190 °C) and $Zn(im)_2$ glass (292 °C).[1, 21] DFT calculations of molecular model complexes support this interpretation, indicating that $Cd^{2+}$ forms weaker coordination bonds with $im^-$ linkers than $Fe^{2+}$, $Co^{2+}$, $Cu^{2+}$, and $Zn^{2+}$ (Figure S5 and Table S2). As a result, $Cd(im)_2$ exhibits lower energy barriers for dissociative processes such as melting and glass transition.

### Modulation of thermal behaviour by linker mixing

Building on the structural and mechanical insights gained from $Cd(im)_2$, we explored an additional strategy to tailor the thermal properties of the Cd-based ZIF by incorporating mixed linkers. The partial substitution of $im^-$ linkers by functionalized derivatives is a well-established approach for modulating the melting and glass formation behavior of ZIFs, as demonstrated in systems such as ZIF-62 ($Zn(im)_{2-x}(bim)_x$, $bim^-$ = benzimidazolate)[3, 15] and ZIF-4-$CN_x$ ($Zn(im)_{2-x}(CNim)_x$, $CNim^-$ = 4-cyanoimidazolate).[2] Here, we applied this strategy to $Cd(im)_2$ by partially replacing $im^-$ by $bim^-$ in the mechanochemical synthesis, yielding $Cd(im)_{2-x}(bim)_x$ compositions with $x$ = 0.05, 0.15, and 0.25 (see Supporting Information Sections 1, 6-7).

Unlike in ZIF-4 ($Zn(im)_2$ or $Co(im)_2$), where partial substitution of $im^-$ by $bim^-$ leads to the formation of ZIF-62, an isoreticular MOF with the same **cag** network topology as ZIF-4, $bim^-$ is unable to fit within the rather dense, interpenetrated $Cd(im)_2$ framework with **dia-c** topology. Consequently, the forced incorporation of $bim^-$ via mechanochemical synthesis introduces additional structural defects and disorder, as evidenced by a pronounced decrease in Bragg peak intensity and an increase in peak widths in the PXRD patterns with increasing $x$. For $Cd(im)_{1.75}(bim)_{0.25}$ (the highest $bim^-$ concentration studied), the PXRD pattern exhibits only weak and broad Bragg reflections corresponding to the crystalline $Cd(im)_2$ phase besides broad diffuse scattering features (Figure 6a). This indicates that $bim^-$ incorporation leads to a highly disordered framework structure with limited crystallographic order. Notably, the PXRD patterns of the $Cd(im)_{2-x}(bim)_x$ materials show additional Bragg reflections associated with residual CdO, suggesting an incomplete mechanochemical reaction. This can be attributed to the incompatibility of $bim^-$ with the crystalline $Cd(im)_2$ structure, further reinforcing the disruptive effect of $bim^-$ incorporation on long-range order.

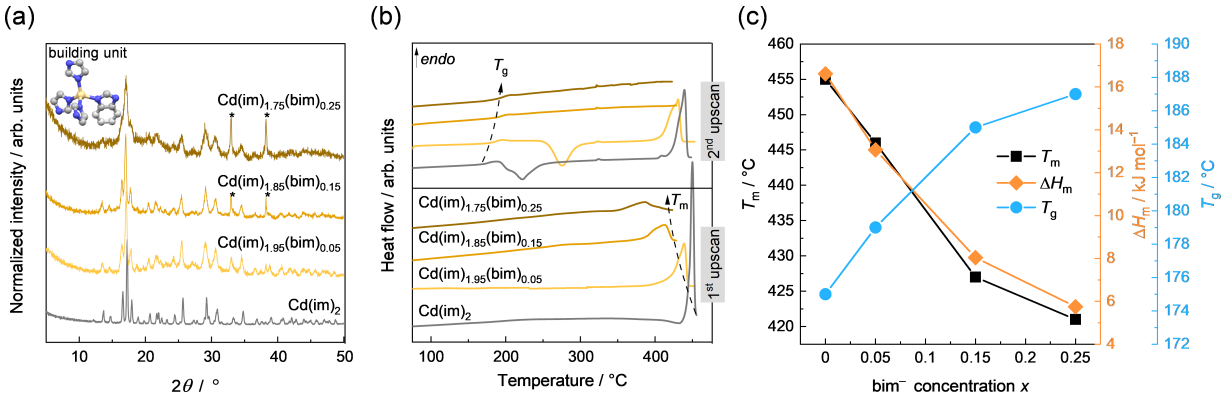


**Figure 6.** (a) PXRD patterns of $Cd(im)_2$ and its mix-linker derivatives $Cd(im)_{2-x}(bim)_x$ with $x$ = 0.05, 0.15 and 0.25. The reflections marked with an asterisk correspond to unreacted CdO. The insert is a schematic of a mixed-linker building unit envisaged for $Cd(im)_{2-x}(bim)_x$. The Cd, N, and C atoms are shown as yellow, blue, and gray spheres, respectively. Hydrogen atoms are omitted for clarity. (b) DSC data of $Cd(im)_2$ and the corresponding $Cd(im)_{2-x}(bim)_x$. The heating and cooling rates for all scans were ±10 °C $min^{-1}$, except for $Cd(im)_2$. (c) Evolution of $T_m$, $\Delta H_m$, and $T_g$ of $Cd(im)_{2-x}(bim)_x$ materials as a function of $x$.

Despite the reduction in crystallinity, DSC analysis reveals that the $Cd(im)_{2-x}(bim)_x$ materials still exhibit clear endothermic signals associated with ZIF melting. With increasing $bim^-$ concentration, the number of defects rises, leading to a gradual decrease in $T_m$ from 455 °C ($x$ = 0) to 421 °C ($x$ = 0.25). Similarly, $\Delta H_m$ decreases from 16.6 kJ $mol^{-1}$ ($x$ = 0) to 5.7 kJ $mol^{-1}$ ($x$ = 0.25) (Figures 6b-c). After cooling the $Cd(im)_{2-x}(bim)_x$ melts to room temperature, ZIF glasses are obtained, as confirmed by the absence of recrystallization signals during cooling of the liquid ZIFs and the presence of $T_g$ signals in a second heating scan. In line with trends observed in the prototypical mixed-linker ZIF-62,[15] $T_g$ gradually increases from 175 °C to 187 °C with increasing $bim^-$ concentration (Figure 6b-c). Moreover, $bim^-$ incorporation in the glassy state effectively suppresses cold-crystallization upon thermal treatment, providing a tunable parameter to control the material's tendency to form glass-ceramics.

## CONCLUSIONS

In this work, we have introduced $Cd(im)_2$ as the first meltable cadmium-based ZIF, synthesized using a mechanochemical synthesis approach. This study expands the family of meltable ZIFs beyond first-row transition metal compounds, providing new insights into the thermal, structural, and mechanical behavior of MOF-derived glasses. Compared to its solution-synthesized counterpart ($Cd(im)_2$-*sol*), mechanochemically synthesized $Cd(im)_2$ features a smaller average crystallite domain size and a higher density of structural defects, leading to a

lower melting temperature and reduced decomposition during melting. Upon rapid cooling, molten $Cd(im)_2$ forms a glass (*g*$Cd(im)_2$), which, upon reheating, undergoes partial recrystallization to yield a semitransparent, single-component glass-ceramic (*prc*$Cd(im)_2$). PDF analysis reveals that while the interpenetrated network structure of crystalline $Cd(im)_2$ is disrupted in its glassy phase, short-range atomic correlations within the individual net persist. During thermal recrystallization, the interpenetrated framework structure gradually reforms, highlighting a unique, reversible structural transition. The glass-ceramic consists of nanocrystals embedded within a glassy matrix of identical composition, forming a complex hybrid crystalline/amorphous microstructure with strong interfacial contact between the two phases.

Nanoindentation studies reveal that *prc*$Cd(im)_2$ exhibits significantly higher hardness and elastic modulus compared to the fully amorphous *g*$Cd(im)_2$. This improvement is attributed to the embedded nanocrystals, which reinforce the glassy matrix, akin to the behavior of conventional inorganic glass-ceramics. The potential to modulate the extent of recrystallization in $Cd(im)_2$ by partial linker substitution and variations in thermal treatment provides a powerful approach for tuning mechanical properties, such as stiffness, hardness, and fracture toughness, in MOF-derived glassy materials. Overall, this study establishes $Cd(im)_2$ as a model system for developing MOF-derived glass-ceramics, demonstrating how mechanochemical synthesis, controlled recrystallization, and linker substitution can be leveraged to fine-tune the properties of MOF glass materials. These findings lay the groundwork for expanding the design space of meltable MOFs, paving the way for novel materials with tailored structural, mechanical, and functional properties.

## ASSOCIATED CONTENT

Supporting Information

Details on materials synthesis, further powder X-ray diffraction (PXRD), synchrotron radiation variable temperature PXRD (VT-PXRD), X-ray total scattering, simultaneous thermogravimetric analysis (TGA) and differential scanning calorimetry (DSC), FTIR and $^1$H NMR spectroscopy, as well as further gas physisorption data, and nanoindentation.

## AUTHOR INFORMATION

*Corresponding Author*

Sebastian Henke*

Email: sebastian.henke@tu-dortmund.de

*ORCID*

Wen-Long Xue: 0000-0003-0778-2300

Alexander Klein: 0000-0002-4963-1626

Mounir El Skafi: 0009-0007-3010-8193

Jan-Benedikt Weiß: 0000-0002-8249-0749

Hui Ding: 0000-0001-5722-0053

Suresh K. Vasa: 0000-0002-8137-9344

Christian Liebscher: 0000-0001-8620-4597

Mirijam Zobel: 0000-0002-8207-8316

Rasmus Linser: 0000-0001-8983-2935

Jin-Chong Tan: 0000-0002-5770-408X

Sebastian Henke: 0000-0003-1502-6038

*Notes*

The authors declare no competing financial interest.

## ACKNOWLEDGMENTS

This paper is adapted from the dissertation of W.-L.X. The Deutsche Forschungsgemeinschaft (project 447344931, HE 7628/7-1) is acknowledged for funding. W.-L.X acknowledges the China Scholarship Council (CSC No. 202008110208). M.E.S. thanks the Oxford-Qatar-Thatcher Graduate Scholarship for postgraduate funding. The Fonds der Chemischen Industrie is gratefully acknowledged for awarding a Kekulé-Fellowship to J.-B.W. The authors thank DELTA Dortmund for allocation of beamtime at beamline BL9 and Dr. Christian Sternemann and Dr. Michael Paulus for their help with the variable temperature PXRD experiments. We thank Diamond Light Source (DLS) for access to beamline I15-1 (CY36120), which contributed to the results presented here. Beamline scientist Philip Chater is acknowledged for their support of the X-ray total scattering experiments at DLS. We thank Guoqiang Li, Pascal Kolodzeiski, Christian Nelle, and Nuttaporn Krittametaporn for their help

with collecting the variable temperature X-ray total scattering data at DLS. The authors gratefully acknowledge the computing time provided on the Linux HPC cluster at Technical University Dortmund (LiDO3), partially funded in the course of the Large-Scale Equipment Initiative by the Deutsche Forschungsgemeinschaft (DFG, German Research Foundation) as project 271512359. We thank Kathrin Ludwigs and Prof. Guido Clever for attempting atomic force microscopy measurements. Robert Jerusalem is acknowledged for the operation of the TEM instrument at TU Dortmund and the analysis of particle sizes. The TEM instrument at TU Dortmund was in part financed by the DFG under grant INST 212/423-1 FUGG.

## REFERENCES

1. Bennett, T. D.; Tan, J. C.; Yue, Y.; Baxter, E.; Ducati, C.; Terrill, N. J.; Yeung, H. H.; Zhou, Z.; Chen, W.; Henke, S.; Cheetham, A. K.; Greaves, G. N., Hybrid glasses from strong and fragile metal-organic framework liquids. *Nat. Commun.* **2015,** *6*, 8079.
2. Song, J.; Frentzel-Beyme, L.; Pallach, R.; Kolodzeiski, P.; Koutsianos, A.; Xue, W.-L.; Schmid, R.; Henke, S., Modulating Liquid–Liquid Transitions and Glass Formation in Zeolitic Imidazolate Frameworks by Decoration with Electron-Withdrawing Cyano Groups. *J. Am. Chem. Soc.* **2023,** *145* (16), 9273-9284.
3. Bennett, T. D.; Yue, Y.; Li, P.; Qiao, A.; Tao, H.; Greaves, N. G.; Richards, T.; Lampronti, G. I.; Redfern, S. A. T.; Blanc, F.; Farha, O. K.; Hupp, J. T.; Cheetham, A. K.; Keen, D. A., Melt-Quenched Glasses of Metal–Organic Frameworks. *J. Am. Chem. Soc.* **2016,** *138* (10), 3484-3492.
4. Ma, N.; Horike, S., Metal–Organic Network-Forming Glasses. *Chem. Rev.* **2022,** *122* (3), 4163-4203.
5. Bennett, T. D.; Horike, S., Liquid, glass and amorphous solid states of coordination polymers and metal–organic frameworks. *Nat. Rev. Mater* **2018,** *3* (11), 431-440.
6. Constable, E. C.; Housecroft, C. E., Coordination chemistry: the scientific legacy of Alfred Werner. *Chem. Soc. Rev.* **2013,** *42* (4), 1429-1439.
7. Cook, T. R.; Zheng, Y.-R.; Stang, P. J., Metal–Organic Frameworks and Self-Assembled Supramolecular Coordination Complexes: Comparing and Contrasting the Design, Synthesis, and Functionality of Metal–Organic Materials. *Chem. Rev.* **2013,** *113* (1), 734-777.
8. Smirnova, O.; Hwang, S.; Sajzew, R.; Ge, L.; Reupert, A.; Nozari, V.; Savani, S.; Chmelik, C.; Reithofer, M. R.; Wondraczek, L.; Kärger, J.; Knebel, A., Precise control over gas-transporting channels in zeolitic imidazolate framework glasses. *Nat. Mater.* **2024,** *23* (2), 262-270.
9. Li, S.; Limbach, R.; Longley, L.; Shirzadi, A. A.; Walmsley, J. C.; Johnstone, D. N.; Midgley, P. A.; Wondraczek, L.; Bennett, T. D., Mechanical Properties and Processing Techniques of Bulk Metal–Organic Framework Glasses. *J. Am. Chem. Soc.* **2019,** *141* (2), 1027-1034.
10. Xue, W.-L.; Kolodzeiski, P.; Aucharova, H.; Vasa, S.; Koutsianos, A.; Pallach, R.; Song, J.; Frentzel-Beyme, L.; Linser, R.; Henke, S., Highly porous metal-organic framework liquids and glasses via a solvent-assisted linker exchange strategy of ZIF-8. *Nat. Commun.* **2024,** *15* (1), 4420.
11. Frentzel-Beyme, L.; Kolodzeiski, P.; Weiß, J.-B.; Schneemann, A.; Henke, S., Quantification of gas-accessible microporosity in metal-organic framework glasses. *Nat. Commun.* **2022,** *13* (1), 7750.
12. McHugh, L. N.; Bennett, T. D., Introducing porosity into metal–organic framework glasses. *J. Mater. Chem. A* **2022,** *10* (37), 19552-19559.

13. Smirnova, O.; Sajzew, R.; Finkelmeyer, S. J.; Asadov, T.; Chattopadhyay, S.; Wieduwilt, T.; Reupert, A.; Presselt, M.; Knebel, A.; Wondraczek, L., Micro-optical elements from optical-quality ZIF-62 hybrid glasses by hot imprinting. *Nat. Commun.* **2024,** *15* (1), 5079.
14. Wang, Y.; Jin, H.; Ma, Q.; Mo, K.; Mao, H.; Feldhoff, A.; Cao, X.; Li, Y.; Pan, F.; Jiang, Z., A MOF Glass Membrane for Gas Separation. *Angew. Chem. Int. Ed.* **2020,** *59* (11), 4365-4369.
15. Frentzel-Beyme, L.; Kloss, M.; Kolodzeiski, P.; Pallach, R.; Henke, S., Meltable Mixed-Linker Zeolitic Imidazolate Frameworks and Their Microporous Glasses: From Melting Point Engineering to Selective Hydrocarbon Sorption. *J. Am. Chem. Soc.* **2019,** *141* (31), 12362-12371.
16. Xue, W.-L.; Li, G.-Q.; Chen, H.; Han, Y.-C.; Feng, L.; Wang, L.; Gu, X.-L.; Hu, S.-Y.; Deng, Y.-H.; Tan, L.; Dove, M. T.; Li, W.; Zhang, J.; Dong, H.; Chen, Z.; Deng, W.-H.; Xu, G.; Wang, G.; Wan, C.-Q., Melt-quenched glass formation of a family of metal-carboxylate frameworks. *Nat. Commun.* **2024,** *15* (1), 2040.
17. Hou, J.; Chen, P.; Shukla, A.; Krajnc, A.; Wang, T.; Li, X.; Doasa, R.; Tizei Luiz, H. G.; Chan, B.; Johnstone Duncan, N.; Lin, R.; Schülli Tobias, U.; Martens, I.; Appadoo, D.; Ari Mark, S.; Wang, Z.; Wei, T.; Lo, S.-C.; Lu, M.; Li, S.; Namdas Ebinazar, B.; Mali, G.; Cheetham Anthony, K.; Collins Sean, M.; Chen, V.; Wang, L.; Bennett Thomas, D., Liquid-phase sintering of lead halide perovskites and metal-organic framework glasses. *Science* **2021,** *374* (6567), 621-625.
18. Banerjee, R.; Phan, A.; Wang, B.; Knobler, C.; Furukawa, H.; O'Keeffe, M.; Yaghi Omar, M., High-Throughput Synthesis of Zeolitic Imidazolate Frameworks and Application to CO2 Capture. *Science* **2008,** *319* (5865), 939-943.
19. Phan, A.; Doonan, C. J.; Uribe-Romo, F. J.; Knobler, C. B.; O'Keeffe, M.; Yaghi, O. M., Synthesis, Structure, and Carbon Dioxide Capture Properties of Zeolitic Imidazolate Frameworks. *Acc. Chem. Res.* **2010,** *43* (1), 58-67.
20. Frentzel-Beyme, L.; Kloß, M.; Pallach, R.; Salamon, S.; Moldenhauer, H.; Landers, J.; Wende, H.; Debus, J.; Henke, S., Porous purple glass – a cobalt imidazolate glass with accessible porosity from a meltable cobalt imidazolate framework. *J. Mater. Chem. A* **2019,** *7* (3), 985-990.
21. León-Alcaide, L.; Christensen, R. S.; Keen, D. A.; Jordá, J. L.; Brotons-Alcázar, I.; Forment-Aliaga, A.; Mínguez Espallargas, G., Meltable, Glass-Forming, Iron Zeolitic Imidazolate Frameworks. *J. Am. Chem. Soc.* **2023,** *145* (20), 11258-11264.
22. Li, S.; Ma, C.; Hou, J.; Yu, S.; Chen, A.; Du, J.; Chater, P. A.; Keeble, D. S.; Qiao, Z.; Zhong, C.; Keen, D. A.; Liu, Y.; Bennett, T. D., Highly porous metal-organic framework glass design and application for gas separation membranes. *Nat. Commun.* **2025,** *16* (1), 1622.
23. Xue, W.-L.; Das, C.; Weiß, J.-B.; Henke, S., Insights into the Mechanochemical Glass Formation of Zeolitic Imidazolate Frameworks. *Angew. Chem. Int. Ed.* **2024**, e202405307.
24. Bumstead, A. M.; Castillo-Blas, C.; Pakamorė, I.; Thorne, M. F.; Sapnik, A. F.; Chester, A. M.; Robertson, G.; Irving, D. J. M.; Chater, P. A.; Keen, D. A.; Forgan, R. S.; Bennett, T. D., Formation of a meltable purinate metal–organic framework and its glass analogue. *Chem. Commun.* **2023,** *59* (6), 732-735.
25. Widmer, R. N.; Lampronti, G. I.; Anzellini, S.; Gaillac, R.; Farsang, S.; Zhou, C.; Belenguer, A. M.; Wilson, C. W.; Palmer, H.; Kleppe, A. K.; Wharmby, M. T.; Yu, X.; Cohen, S. M.; Telfer, S. G.; Redfern, S. A. T.; Coudert, F. X.; MacLeod, S. G.; Bennett, T. D., Pressure promoted low-temperature melting of metal-organic frameworks. *Nat. Mater.* **2019,** *18* (4), 370-376.
26. Peng, S.-X.; Yin, Z.; Zhang, T.; Yang, Q.; Yu, H.-B.; Zeng, M.-H., Vibration assisted glass-formation in zeolitic imidazolate framework. *J. Chem. Phys.* **2022,** *157* (10), 104501.
27. Thorne, M. F.; Gómez, M. L. R.; Bumstead, A. M.; Li, S.; Bennett, T. D., Mechanochemical synthesis of mixed metal, mixed linker, glass-forming metal–organic frameworks. *Green Chem.* **2020,** *22* (8), 2505-2512.

28. Thorne, M. F.; Sapnik, A. F.; McHugh, L. N.; Bumstead, A. M.; Castillo-Blas, C.; Keeble, D. S.; Diaz Lopez, M.; Chater, P. A.; Keen, D. A.; Bennett, T. D., Glassy behaviour of mechanically amorphised ZIF-62 isomorphs. *Chem. Commun.* **2021,** *57* (73), 9272-9275.
29. Collings, I. E.; Cairns, A. B.; Thompson, A. L.; Parker, J. E.; Tang, C. C.; Tucker, M. G.; Catafesta, J.; Levelut, C.; Haines, J.; Dmitriev, V.; Pattison, P.; Goodwin, A. L., Homologous Critical Behavior in the Molecular Frameworks Zn(CN)2 and Cd(imidazolate)2. *J. Am. Chem. Soc.* **2013,** *135* (20), 7610-7620.
30. Lehnert, R.; Seel, F., Darstellung und Kristallstruktur des Mangan(II)- und Zink(II)-Derivates des Imidazols. *Z. Anorg. Allg. Chem.* **1980,** *464* (1), 187-194.
31. Qiao, A.; Bennett, T. D.; Tao, H.; Krajnc, A.; Mali, G.; Doherty, C. M.; Thornton, A. W.; Mauro, J. C.; Greaves, G. N.; Yue, Y., A metal-organic framework with ultrahigh glass-forming ability. *Sci. Adv.* **2018,** *4* (3), eaao6827.
32. Holand, W.; Beall, G. H., *Glass-ceramic technology*. John Wiley & Sons: 2019.
33. Hou, J.; Ashling, C. W.; Collins, S. M.; Krajnc, A.; Zhou, C.; Longley, L.; Johnstone, D. N.; Chater, P. A.; Li, S.; Coulet, M.-V.; Llewellyn, P. L.; Coudert, F.-X.; Keen, D. A.; Midgley, P. A.; Mali, G.; Chen, V.; Bennett, T. D., Metal-organic framework crystal-glass composites. *Nat. Commun.* **2019,** *10* (1), 2580.
34. Ryder, M. R.; Civalleri, B.; Bennett, T. D.; Henke, S.; Rudić, S.; Cinque, G.; Fernandez-Alonso, F.; Tan, J.-C., Identifying the Role of Terahertz Vibrations in Metal-Organic Frameworks: From Gate-Opening Phenomenon to Shear-Driven Structural Destabilization. *Phys. Rev. Lett.* **2014,** *113* (21), 215502.
35. Madsen, R. S. K.; Qiao, A.; Sen, J.; Hung, I.; Chen, K.; Gan, Z.; Sen, S.; Yue, Y., Ultrahigh-field 67Zn NMR reveals short-range disorder in zeolitic imidazolate framework glasses. *Science* **2020,** *367* (6485), 1473-1476.
36. Brouwer, D. H., 9.06 - Applications of silicon-29 NMR spectroscopy. In *Compr. Inorg. Chem. III*, Reedijk, J.; Poeppelmeier, K. R., Eds. Elsevier: Oxford, 2023; pp 107-137.
37. Farrow, C. L.; Juhas, P.; Liu, J. W.; Bryndin, D.; Božin, E. S.; Bloch, J.; Proffen, T.; Billinge, S. J. L., PDFfit2 and PDFgui: computer programs for studying nanostructure in crystals. *J. Phys.: Condens. Matter* **2007,** *19* (33), 335219.
38. Tan, J.-C., Fundamentals of MOF Mechanics & Structure–Mechanical Property Relationships. In *Mechanical Behaviour of Metal – Organic Framework Materials*, Tan, J.-C., Ed. The Royal Society of Chemistry: 2023; pp 1-64.
39. Varshneya, A. K.; Mauro, J. C., *Fundamentals of Inorganic Glasses*. Elsevier: 2019.
40. Wondraczek, L.; Bouchbinder, E.; Ehrlicher, A.; Mauro, J. C.; Sajzew, R.; Smedskjaer, M. M., Advancing the Mechanical Performance of Glasses: Perspectives and Challenges. *Adv. Mater.* **2022,** *34* (14), 2109029.
41. Tricarico, M.; Tan, J.-C., Nanostructure-dependent indentation fracture toughness of metal-organic framework monoliths. *Next Mater.* **2023,** *1* (1), 100009.

## TOC Graphic